Predicting Helicopter Damage Caused by a Collision with an Unmanned Aerial System Using Explicit Finite Element Analysis

Jonkheijm, L.; Chen, B. Y.; Schuurman, M.J.

DOI
10.2514/6.2022-1486

Publication date
2022

Document Version
Final published version

Published in
AIAA SCITECH 2022 Forum

AIAA SciTech Forum
January 3-7, 2022, San Diego, CA & Virtual
AIAA SCITECH 2022 Forum

10.2514/6.2022-1486

Predicting Helicopter Damage Caused by a Collision with a UAS Using Explicit FEA

Laurens Jonkheijm*, Boyang Chen†, Michiel Schuurman‡
Delft University of Technology, Faculty of Aerospace Engineering, Kluyverweg 1, 2629HS, Delft, the Netherlands.

With the rising number of Unmanned Aerial Systems (UAS) flying in the sky, an increase in collisions with manned aircraft seems inevitable. Since these devices are permitted to operate in airspace which they share with rotorcraft, a helicopter is certainly not retained from the risk of colliding with a UAS. The only prevailing impact related certification requirement for rotorcraft is the §29.631, which is only applicable to all larger (Part 29) rotorcraft. This requirement states that the rotorcraft must be capable of safe continuation of the flight and/or safe landing after an impact with a 1 kg bird up to the rotorcraft's maximum horizontal velocity. In this paper, simulations have been performed in explicit Finite Element software to assess how much damage a Part 29 compliant helicopter would sustain after colliding with a UAS. For this purpose, an Agusta A-109 helicopter windshield was impacted by a DJI Phantom III quadcopter UAS under various conditions. The results of the simulations showed that the windshield would sustain severe damage after the impact. Not only would the windshield break into dangerous fragments that could enter the cockpit, parts of the UAS would also penetrate the windshield. These items could strike the crew and a safe continuation of the flight and/or safe landing following the impact cannot be guaranteed. A similar level of safety compared to the bird strike requirement in the prevailing certification requirement is therefore not assured.

I. Nomenclature

CAD	=	Computer Aided Design
CS	=	Certification Specification
EASA	=	European Aviation Safety Agency
EOS	=	Equation Of State
FAA	=	Federal Aviation Administration
FE	=	Finite Element
FEA	=	Finite Element Analysis
MMPDS	=	Metallic Materials Properties Development and Standardization
SPH	=	Smoothed Particle Hydrodynamics
S/R	=	Selectively Reduced
UAS	=	Unmanned Aerial System

II. Introduction

Due to technological innovations in the Unmanned Aerial System (UAS) industry, the potential for recreational as well as commercial purposes of these devices has increased remarkably. Due to an accompanying reduction in the price of the systems, the number of shipments has increased exponentially over the last few years and this growth is expected to continue even further in the upcoming years [1]. The Federal Aviation Administration (FAA) permits UAS operators to fly their device without pre-flight operating approval in the uncontrolled Class G airspace and up to 400 ft Above Ground Level [2]. Helicopters most frequently operate within this airspace and regularly operate below the UAS upper limit of 400 ft. This is particularly applicable to military and other helicopters in governmental service, because these helicopters fly and land wherever the operation requires them to do so. Since many UAS owners are either not

*MSc Graduate, Aerospace Structures & Materials Department, L.Jonkheijm@tudelft.nl, non-member.
†Assistant Professor, Aerospace Structures & Materials Department, B.Chen-2@tudelft.nl, non-member.
‡Assistant Professor, Aerospace Structures & Materials Department, M.J.Schuurman@tudelft.nl, AIAA member.

aware of the imposed regulations or consciously choose to ignore them, the number of proximity incidents between UAS and manned aircraft in the United Kingdom alone has more than doubled from 40 in 2015 to 94 in 2016 [3].

Due to the increasing number of proximity incidents and the regularity of helicopter operations in airspace shared with UAS pilots, the question arises how much damage a helicopter could sustain following a collision with a UAS. The aim of this research was to gain more insight into the answer to this question, since the current state of art focused on UAS to fixed wing aircraft encounters.

In the design of a rotorcraft, the sole impact related prevailing Certification Specification (CS) of the FAA and the European Aviation Safety Agency (EASA) applies to the larger rotorcraft (Part 29) and is the CS §29.631 [4, 5]: *"The rotorcraft must be designed to ensure capability of continued safe flight and landing (for Category A) or safe landing (for Category B) after impact with a 1 kg bird, when the velocity of the rotorcraft is equal to Vne or Vh."*. To answer the research question, an assessment has been made to determine the damage that a helicopter compliant with this CS would sustain following a collision with a UAS. This assessment has been completed by performing simulations in Finite Element (FE) software.

III. FE Models

The generalized equation of motion (damping ignored) of a system for Finite Element Analysis (FEA) is: $M\ddot{U} + KU = R$ in which M and K are respectively the mass and stiffness matrices and $\ddot{U}$, U and R, the nodal accelerations, displacements and applied nodal force vectors. To solve this system, an explicit integration method can be enforced, which calculates the state of the system at the next time increment $(t + \Delta t)$ from the state at the current time (t). Since no iteration is required in explicit FEA, the method is more computationally efficient at each time step when compared to the other widely used integration method, the implicit integration scheme. The state of the system in the implicit method is namely calculated through iteration based on the current state (t) and the state at the next increment $(t + \Delta t)$. However, the implicit method is unconditionally stable whilst in an explicit solver, the time step should be sufficiently small to guarantee stability. An explicit solver is generally more computationally efficient for dynamic problems involving higher strain rates, which is the case in the problem in this paper.

For this reason, the LS Dyna explicit FEA solver was used in this research to perform the various simulations. To guarantee stability in this explicit solver [6], the time step (Δt) in LS Dyna is automatically set as follows: $\Delta t = S_{ts} \cdot \Delta t_{crit}$ in which S_{ts} is a user defined scale factor for the time step (default to 0.9) and Δt_{crit} is the critical time step. This critical time step is calculated as follows: $\Delta t_{crit} = l_{char}/c$ in which l_{char} is the characteristic length of an element and c the speed of sound. The characteristic length is governed by the shape and size of the element, whilst the material properties of the element define the speed of sound. LS Dyna calculates the critical time step of each element in the simulation and uses the smallest value to set the actual time step. The material properties of each part in the simulation are represented in LS Dyna by a material card. This material card fills the stiffness matrix K, which will not be constant during the load application, since the strains will exceed the linear regime.

In case no additional information is provided below, the default values of LS Dyna were adopted in the simulation. Apart from the bird model in the bird strike analysis, (Paragraph III.B.2), a Lagrangian numerical formulation was used throughout. For the parts composed of these Lagrangian elements, contact between the various parts was defined by adopting the penalty based *CONTACT_AUTOMATIC_SURFACE_TO_SURFACE algorithm.

A. DJI Phantom III

The DJI Phantom family is by a considerable margin the most popular UAS among recreational operators. Due to availability of validation data of the critical components of the DJI Phantom III, this UAS was selected as the impacting body within this study.

1. FE Model

An accurate Computer Aided Design (CAD) model of the external geometry of the DJI Phantom III was available at the free library of GrabCAD.com [7]. A simplified homogeneous box was inserted into the main body to represent the battery, thereby omitting for example the presence of the casing of the battery. All other internal components, such as circuit boards and wiring, were not incorporated in the model. The mass of these components was added to the main body as non-structural mass through the LS Dyna *ELEMENT_MASS function to ensure that the mass of the entire UAS matched the actual mass of the DJI Phantom III. This guaranteed that the kinetic energy of the impacting body, which is an essential variable of importance in impact mechanics, is similar to the kinetic energy of the actual device.

The camera was also considered a homogeneous body, thereby omitting the internal parts of this component and adding its mass as non-structural mass to the camera body to match the part with the recorded values during the validation tests as detailed in Table 5.

For each UAS component, a mesh sensitivity analysis was performed to determine the most optimal compromise between accuracy of the results and computational time required. The mesher type as well as the selected element size is detailed in Figure 1. For the critical components (i.e. battery, motors, and camera), 3D solid elements with selectively reduced (S/R) integration were adopted. To save computational time on the remaining non critical bulk item, the camera gimbal was represented by constant stress solid elements. Fully integrated shell elements were selected for the main body and propellers due to the thin walled geometry of these components.

Table 1 Metallic material properties (MMPDS [8]).

Material Property	Symbol	A520.0-F	AISI 4130	Unit
Density	ρ	2600	7850	kg/m^3
Modulus of Elasticity	E	66	200	GPa
Poisson's Ratio	ν	0.33	0.32	-
Yield Stress	σ_y	170	483	MPa
Tangent modulus	E_t	1164	1174	MPa
Failure strain	ϵ_{max}	0.14	0.12	-

The camera casing and the rotor of the motors were made out of aluminium alloy A520.0-F, whilst AISI 4130 steel alloy was the material of the core stator of the motor. These metals were represented by a bilinear stress-strain relationship through the LS Dyna *MAT_PIECEWISE_LINEAR_PLASTICITY material card. The material properties have been obtained from the Metallic Materials Properties Development and Standardization (MMPDS) database [8] and are listed in Table 1. Material properties of various lithium-ion pouch cells were established by Sahraei, Meier and Wierzbicki [9] and the properties applicable to the cells of the battery of the DJI Phantom III are listed in Table 2. The material was represented by the *MAT_CRUSHABLE_FOAM option in which an arbitrary load curve defined the relationship between the yield stress and volumetric strain. For the polycarbonate of the main body, propellers, and camera gimbal, Meng et al. [10] performed various tests and the established material properties are detailed in Table 3. The *MAT_PLASTIC_KINEMATIC LS Dyna card was adopted for this material and was configured to represent an elastic-plastic model with ideal plasticity. The failure strain was added to the various material models through the *MAT_ADD_EROSION option. Once the failure strain in a certain element was satisfied, this element was deleted from the calculation. An overview of the FE model of the entire DJI Phantom III model is shown in Figure 1.

Table 2 Lithium-ion battery material properties (Sahraei, Meier and Wierzbicki [9]).

Material Property	Symbol	Value	Unit
Density	ρ	1750	kg/m^3
Modulus of Elasticity	E	500	GPa
Poisson's Ratio	ν	0.01	–
Compressive Stress	σ	$276{\cdot}\epsilon^{1.8}$	MPa
Failure strain	ϵ_{max}	0.16	-
Tensile cut off	Y_t	30	MPa

Table 3 Polycarbonate material properties (Meng et al. [10]).

Material Property	Symbol	Value	Unit
Density	ρ	1180	kg/m^3
Modulus of Elasticity	E	2.35	GPa
Poisson's Ratio	ν	0.3	-
Yield Stress	σ_y	62	MPa
Failure strain	ϵ_{max}	0.2	-

2. Validation tests

Olivares et al. [11] performed a number of actual tests impacting the critical components (i.e. battery, motors, and camera) of the UAS onto the center of an aluminium plate for validation purposes of their DJI Phantom III FE model. The results of these tests were used in this study for the same purpose, namely to validate the FE model of the critical components as created above in Paragraph III.A.1.

In the actual tests, an aluminium alloy 2024-T3 target plate of constant thickness was sandwiched in between two square-shaped steel frames, which were bolted together. The area of the plate inside the opening of the frames and therefore exposed to the projectile was 890 by 890 mm. In the FE simulations representing this test set-up, the target plate was a surface plane measuring the exposed area with clamped boundary conditions imposed at the edges of this plane to represent the surrounding structure. LS Dyna default Belytschko-Tsay shell elements were selected (element

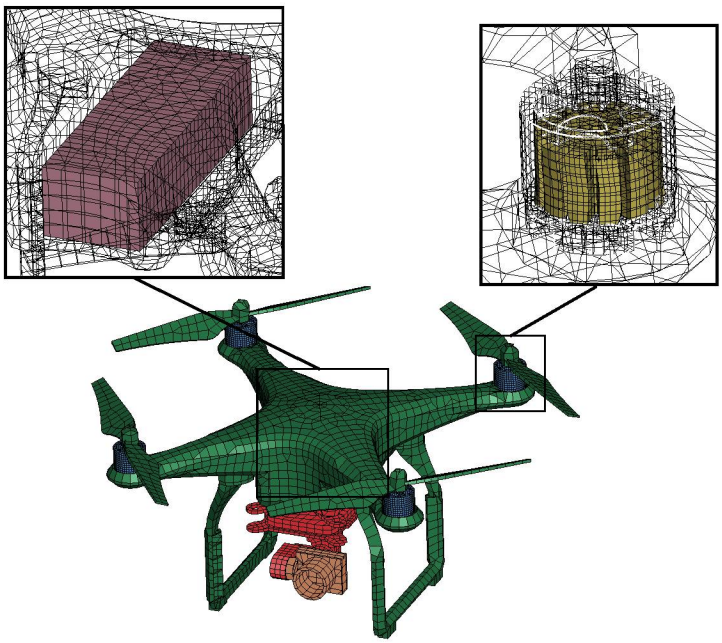

UAS component	LS Dyna material model	Material	LS Dyna element type	LS Dyna mesher
Main body	Plastic Kinematic (*MAT_003)	Polycarbonate (Table 3)	Shell fully integrated (ELFORM 16)	Auto shell mixed type Element size 8 mm
Camera gimbal	Plastic Kinematic (*MAT_003)	Polycarbonate (Table 3)	Solid constant stress (ELFORM 1)	Auto solid Element size 5 mm
Camera	Piecewise Linear Plasticity (*MAT_024)	A520.0-F (Table 1)	Solid with S/R integration (ELFORM 2)	Auto solid Element size 8 mm
Motor rotor	Piecewise Linear Plasticity (*MAT_024)	A520.0-F (Table 1)	Solid with S/R integration (ELFORM 2)	Auto solid Element size 2 mm
Motor stator	Piecewise Linear Plasticity (*MAT_024)	AISI 4130 (Table 1)	Solid with S/R integration (ELFORM 2)	Auto solid Element size 2 mm
Battery	Crushable Foam (*MAT_063)	Lithium-ion cells (Table 2)	Solid with S/R integration (ELFORM 2)	Box Solid 9.1×6.8×4.3 mm

Fig. 1 DJI Phantom III FE model overview.

Table 4 Aluminium 2024-T3 material properties (Kay [12]).

Material Property	Symbol	Value	Unit	Material Property	Symbol	Value	Unit
Density	ρ	2770	kg/m^3	Strain hardening coefficient	B	684.0	MPa
Modulus of Elasticity	E	72	GPa	Strain rate coefficient	C	0.0083	-
Poisson's Ratio	ν	0.33	-	Thermal softening exponent	m_t	1.7	-
Strain hardening constant	A	369.0	MPa	Strain hardening exponent	n	0.73	-

Johnson-Cook failure parameters [-]

D_1	D_2	D_3	D_4	D_5
0.112	0.123	1.500	0.007	0.0

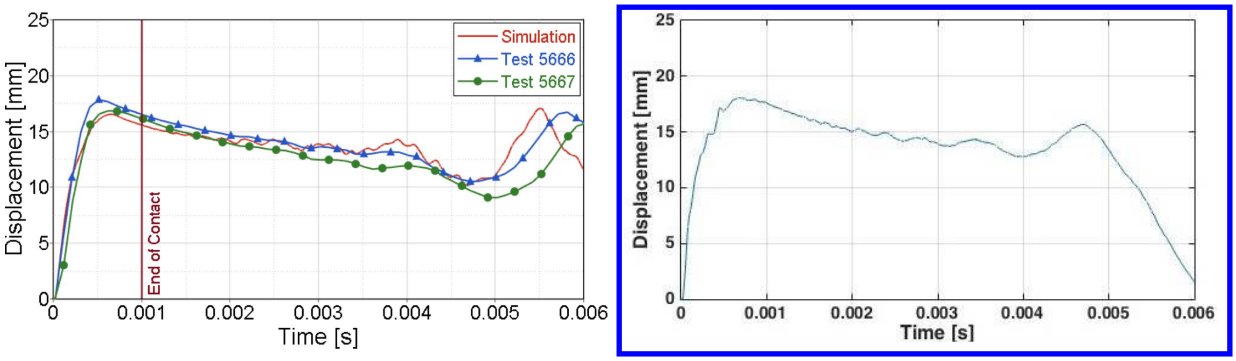

(a) Ballistic test results (Olivares et al. [11])

(b) FEM model simulation

Fig. 2 Verification of center displacement of a 1.6 mm thick A2024-T3 panel impacted by the camera at 128.6 m/s.

formulation 2) and the 2024-T3 aluminium material model as established by Kay [12] was adopted. In this model, the aluminium was represented by a Johnson-Cook failure strain model and the material properties are presented in Table 4. These properties were incorporated in the LS Dyna *MAT_JOHNSON_COOK strain rate and temperature sensitive material model (*MAT_015).

During this validation process, the deflection of the center of the target plate in the simulations has been compared with the results of the actual tests. An example of the camera impacting a 1.6 mm thick panel at 128.6 m/s is shown in Figure 2. Additionally a visual representation of the FE simulation has been compared with images from the actual test to assess how accurately the deformation of the UAS components and the target plate as well as the contact between the two was captured. An example of this step for the motor impacting a 1.6 mm thick panel at 128.6 m/s is shown in Figure 3.

When analysing the results, the motors and camera showed a strong correlation with the actual test results. The initial and subsequent deflection of the center of the target plate was accurately captured. Additionally, contact between the two components as well as the deformation of the UAS component in the simulation closely matched the actual test results. However, although the initial deformation was accurately captured for the battery impact, the subsequent deformation was consistently slightly under predicted in the simulations. After initial contact, the mechanism of disintegration of the battery in the simulations deviated from the actual test results. The correlation between the actual test results and the simulations for the battery was therefore moderate. Since the battery suffered from a complete disruption, the adopted Lagrangian mesh inaccurately captured the sustained large deformations, which is a typical challenge for this mesh type. A summary of the results of the validation process of the various components is presented in Table 5.

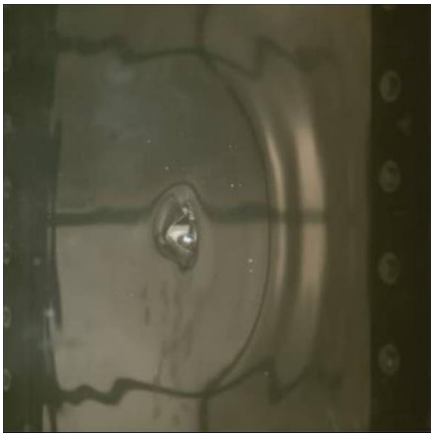

(a) Ballistic test at 1 ms (Olivares et al. [11])

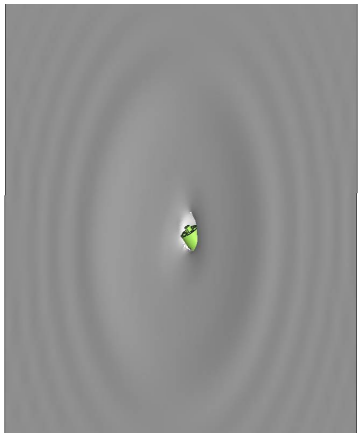

(b) FEM model simulation at 1 ms

Fig. 3 Comparison of the damage propagation of a 1.6 mm thick A2024-T3 panel impacted by the motor at 128.6 m/s at different time intervals.

Table 5 Results of the validation process of the DJI Phantom III critical components.

UAS component	Plate thickness [mm]	Impact velocity [m/s]	Projectile weight [g]	Penetration of projectile		Max plate deflection [mm]		Simulation correlation
				Actual[1]	Sim	Actual[1]	Sim	
Battery	1.6	127.71	343.07	No	No	47.8	51.8	Moderate
Battery	6.35	131.67	350.06	No	No	19.6	20.7	Moderate
Battery	3.18	49.68	344.1	No	No	14.5	17.6	Moderate
Motor	1.6	128.32	50.73	Yes	Yes	N/A	N/A	Strong
Motor	6.35	136.25	50.98	No	No	7.9	7.6	Strong
Camera	1.6	129.24	52.57	No	No	18.5	18.1	Strong

[1] Test results performed by Olivares et al. [11]

B. Helicopter windshield

Based on a probability analysis, the windshield of a helicopter was selected within this study as the impact location and specifically the Agusta 109 helicopter (A-109) as a representative helicopter windshield. This selection was based on the fact that its windshield material properties as well as a CAD model of the entire aircraft was available. Details of the surrounding structure of the windshield was not accessible, therefore the model only comprised of the windshield itself and boundary conditions were imposed at the edges. All impacts in this study were simulated onto the left hand cockpit windshield of the helicopter.

1. FE Model

In the free CAD library of GrabCAD.com [13], a model of the entire A-109 was available which has been compared with the dimensions of the fuselage of the actual aircraft. After scaling the CAD model, the difference between the two was minor and it was assumed that the dimension of the windshield would also match with a similar accuracy.

Table 6 Stretch acrylic material properties (Hedayati et al. [14]).

Material Property	Symbol	Value	Unit
Density	ρ	1180	kg/m^3
Modulus of Elasticity	E	3.17	GPa
Poisson's Ratio	ν	0.4	-
Yield stress	σ_y	73	MPa
Hardening parameter	β	0.5	-
Failure strain	ϵ_{max}	0.023	-

Based on the best compromise between computational time required and accuracy of the results, the optimal mesh was for a default element size of 3.5 mm using the shell mixed type mesher of LS Dyna. To prevent hourglassing modes, the fully integrated shell element formulation was adopted. The windshield of the A-109 simulated in this study had a single layer stretch acrylic lay-up and the material properties were obtained from Hedayati et al. [14], refer to Table 6. These properties were inserted into the *MAT_PLASTIC_KINEMATIC card, which was configured to represent an elastic perfectly plastic behaviour of the material. Strain rate effects were considered by implementing the Cowper-Symonds model, which scales the yield stress as follows [6]: $\sigma_d/\sigma_s = 1 + (\dot{\epsilon}/C_{cs})^{1/p}$ in which σ_d is the dynamic and σ_s the static yield stress. $\dot{\epsilon}$ is the strain rate and C_{cs} and p are the Cowper-Symonds parameters. For the acrylic, values of C_{cs} = 40 1/s and p = 4 were implemented in the material card.

No information was available on the surrounding structure of the windshield of the A-109 and therefore it was unknown how to represent this structure realistically. The single option was to impose boundary conditions on the edges of the windshield to represent the surrounding structure. To assess the sensitivity of the results of the simulations with respect to the imposed boundary conditions, two sets of boundary conditions as shown in Figure 4 were created. In the first configuration, all rotations (θ) and translations (T) at the edges were fixed thereby clamping the windshield as adopted by most of the related published literature such as for example in the report of Hedayati et al. [14]. In the second configuration, only the in-plane translations were constrained at the edges adjacent the right hand cockpit windshield and the overhead windshield, whilst the other edges remained to be clamped. This is based on the assumption that during the impact of the windshield, these adjacent windshields would be loaded in tension and thereby provide in-plane stiffness, which could be valid for relatively small deformations. This would represent a more flexible surrounding structure when compared to the clamped boundary conditions, which is potentially more realistic for a more compact rotorcraft. An overview of the FE model of the helicopter windshield is shown in Figure 5.

2. Bird strike analysis

A literature review showed that no results of validation tests for rotorcraft windshields were freely available. As an alternative approach to determine a representative thickness of the windshield, simulations were performed to establish a windshield that complied with the prevailing certification requirements. As stated in Paragraph II, the only prevailing certification requirement of the FAA and EASA was the 1 kg bird strike requirement of §29.631 [4, 5]. Although the A-109 is actually a Part 27 aircraft and therefore this requirement does not apply, the FE model of the windshield in this study was created as if it would comply with the Part 29 requirement. With respect to an actual smaller Part 27 compliant rotorcraft, the resulting damage of the simulations would be conservative. However, the Part 29 bird strike requirement was the only source of guidance.

Table 7 Bird tabulated equation of state parameters (Grimaldi [15]).

ϵ_V [-]	C [MPa]	ϵ_V [-]	C [MPa]
0	0	-0.154	972
-0.105	237	-0.169	1180
-0.118	425	-0.183	1370
-0.128	586	-0.195	1540
-0.137	727	-0.217	1840

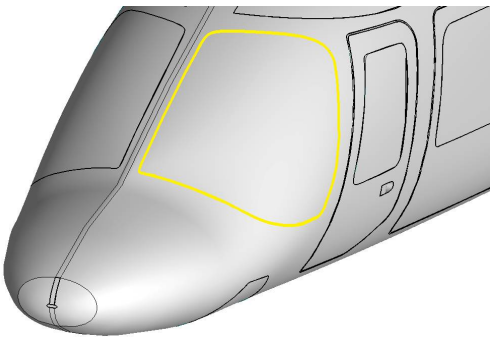

(a) Clamped boundary conditions.

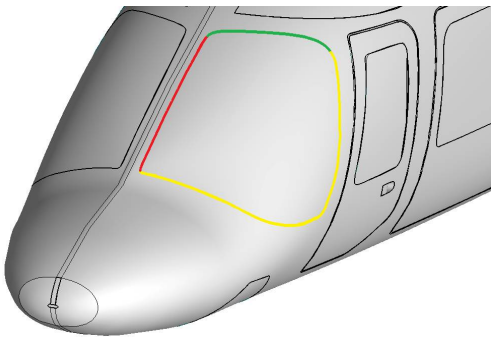

(b) Alternative boundary conditions.

Linecolor	T_x	T_y	T_z	θ_x	θ_y	θ_z
	0	0	0	0	0	0
	0	1	1	1	1	1
	1	0	1	1	1	1

0 = Constraint degree of freedom, 1 = Unconstraint degree of freedom

Fig. 4 Windshield various configurations of boundary conditions.

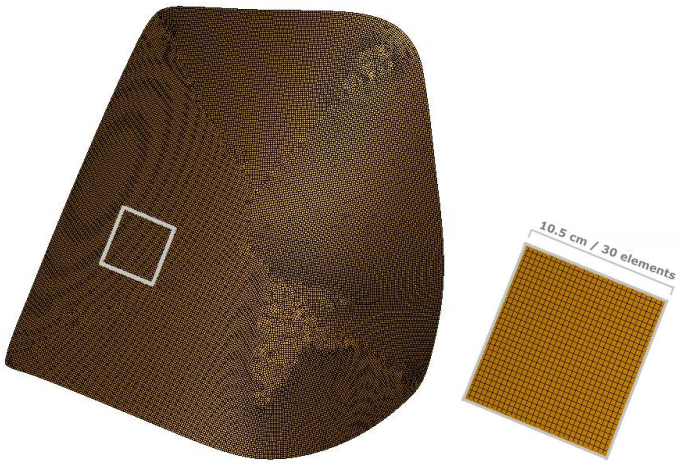

Helicopter component	Windshield
LS Dyna material model	Plastic Kinematic (*MAT_003)
Material	Polycarbonate (Table 6)
LS Dyna element type	Shell fully integrated (ELFORM 16)
LS Dyna mesher	Auto shell mixed type Element size 3.5 mm

Fig. 5 Helicopter windshield FE model overview.

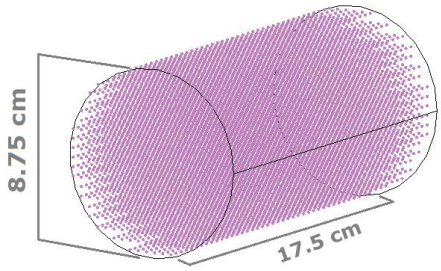

Fig. 6 Bird SPH model.

A Smoothed Particle Hydrodynamics (SPH) bird model based on the model from Grimaldi [15] was incorporated in the simulations. In this model, the bird was simplified by a cylindrical shape with a mass density of 950 kg/m^3 and a 2:1 length (17.5 cm) to diameter (8.75 cm) ratio to match the 1 kg of the certification requirement. The selected material model was the *MAT_NULL card (*MAT_009) which allows an Equation Of State (EOS) to be considered without computing deviatoric stresses. The EOS added to this material model was the *EOS_TABULATED card in which the pressure P is calculated as follows: $P = C(\epsilon_V)$. In this equation is $C(\epsilon_V)$ the tabulated pressure as a function of the volumetric strain ϵ_V and LS Dyna linearly interpolates between the tabulated values. The EOS parameters as listed in Table 7 were inserted in the EOS card. The model contained a total of 12640 particles as shown in Figure 6. The bird impacted the windshield at the same location as the UAS battery as shown in Figure 7 at the maximum cruising velocity of the A-109 of 156 kts ($\approx$ 80 m/s). Contact between the Lagrangian elements of the windshield and the SPH nodes of the bird was established through the penalty based *CONTACT_AUTOMATIC_NODES_TO_SURFACE algorithm.

The results of the simulations showed that 9.3 mm was the minimum thickness for the acrylic windshield with clamped edges to ensure that the bird did not penetrate the windshield and the windshield did not break into dangerous fragments. For the alternative set of boundary conditions, these conditions were met at a reduced windshield thickness of 6.6 mm. The crew would be protected and a safe landing in accordance with the certification requirement would be guaranteed under these conditions. The results indicated that a thinner windshield would be required in case less stringent boundary conditions are imposed onto the edges of the windshield. A thinner windshield would therefore comply with the requirements in case the surrounding structure is more flexible.

IV. UAS collision results

A. Test set-up

To allow a direct comparison with the prevailing certification requirements, the test set-up was configured to match the conditions as defined in the CS §29.631 [4, 5] replacing the 1 kg bird with the UAS model. The impact velocity was therefore set to the maximum cruising velocity of the A-109 of 80 m/s. The impact location of the UAS was aligned horizontally such that all four motors contacted the windshield and vertically such that the battery would strike the windshield's center. The battery impact location matched the impact location of the bird during the bird strike analysis (Paragraph III.B.2) to allow for a direct comparison between the two. An overview of the test set-up is presented in Figure 7. In the various simulations, contact was only defined between the various UAS components and the target windshield, whilst contact among the various UAS components themselves was not incorporated. This reduced the computational time required, but would not have a significant effect on the results due to the fact that the various components in sequence contacted the target due to the relative inclination. The reader might though observe some components unnaturally passing through each other after contact with the windshield.

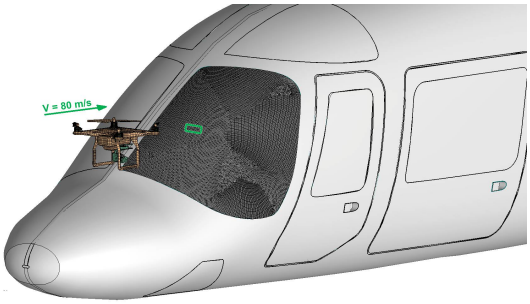

Impact location of the UAS battery. Windshield surrounding structure is only displayed for visualization purposes and was not incorporated in the simulation.

Fig. 7 Helicopter windshield UAS impact simulation overview.

B. Damage assessment

1. UAS Impact

To assess the extent of the damage the windshield would sustain after a UAS impact, the DJI Phantom III was impacted onto a windshield that would comply with the certification requirements for Part 29 aircraft. For the clamped

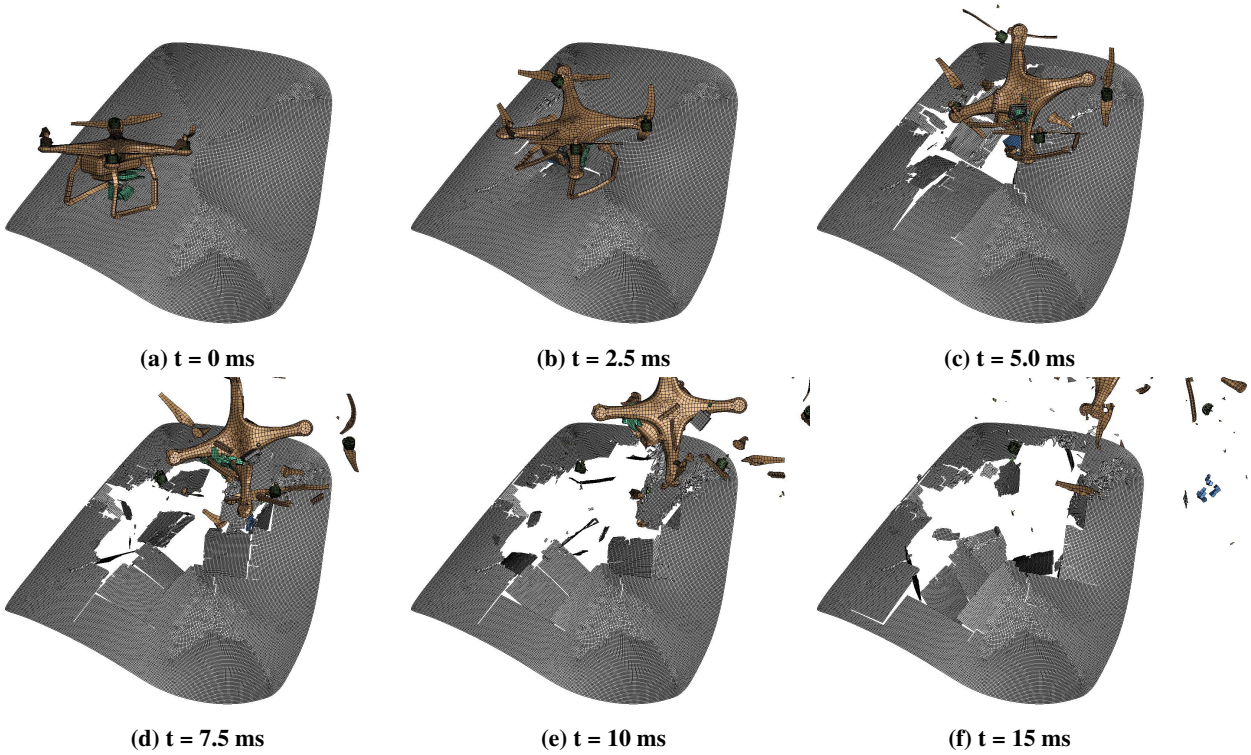

(a) t = 0 ms (b) t = 2.5 ms (c) t = 5.0 ms

(d) t = 7.5 ms (e) t = 10 ms (f) t = 15 ms

Fig. 8 Damage propagation of a 9.3 mm thick windshield with clamped edges impacted by the UAS.

boundary conditions, this would be the case for the A-109 windshield model with a thickness of 9.3 mm. The results of the simulations of the UAS impact onto this windshield will be discussed, whilst a comparison with the other boundary conditions will be presented in Paragraph IV.B.2. The visual representation of the results of this simulation is shown in Figure 8.

After the battery and camera initiated the damage at the impact location, the damage propagated over the entire windshield. At the end of the simulation, only the edges of the windshield remained intact and attached to the surrounding frame, which was simplified by the imposed the boundary conditions. The windshield broke into dangerous fragments which entered the cockpit. Additionally, the battery and main body of the UAS partly penetrated the windshield and entered the cockpit whilst the other parts deflected away from the windshield.

Based on the simulations, it can be concluded that a Part 29 compliant windshield would sustain severe damage after an impact with the DJI Phantom III. The §29.631 CS [4, 5] required that continued safe flight and/or landing must be guaranteed after impact with a 1 kg bird. For a collision with the DJI Phantom III under these conditions, a similar level of safety could not be guaranteed since fragments of the windshield as well as parts of the UAS would enter the cockpit and could strike the cockpit crew.

The crack propagation of the windshield in the various results of the simulations was predominantly along straight lines, which was a discrepancy when compared to actual damaged acrylic windshields. This mesh bias was a result of the default mixed mode mesher type of LS Dyna, which mainly adopted quadrilateral elements in this specific geometry. By switching to the triangular mesher in the software, a more realistic (curved) crack pattern was established in the simulations. However, the sustained damage was of a similar size and therefore it was concluded that the resulting damage and the subsequent conclusions would not be sensitive to the mesh type. Solutions to reduce the effect of this bias are for example to adopt an Extended FE or floating node method .

2. Boundary conditions

Due to unavailability of information regarding the surrounding structure of the windshield, two configurations of boundary conditions (Figure 4) were imposed at the edges of the windshield to assess the sensitivity of the results of the simulations with respect to the imposed boundary conditions. For the clamped boundary conditions, a 9.3 mm

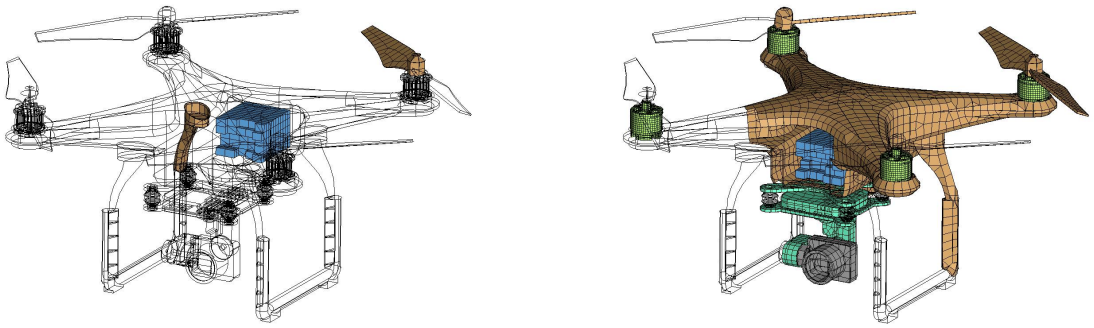

(a) Clamped boundary conditions. Windshield thickness is 9.3 mm.

(b) Alternative boundary conditions. Windshield thickness is 6.6 mm.

The covered parts in these figures penetrated the windshield.

Fig. 9 Comparison of the UAS parts penetrating a Part 29 compliant windshield for various windshield boundary conditions.

thick windshield complied with the certification requirements, whilst the thinner 6.6 mm thick windshield guaranteed compliance for the alternative set of boundary conditions (Paragraph III.B.2).

For the compliant windshields of both sets of boundary conditions, the parts of the UAS that penetrated into the cockpit during the collision are shown in Figure 9. The damage of the windshield caused by the collision was of a similar size for both configurations of boundary conditions. However, the number of parts penetrating the windshield differed significantly between the two tested configurations. For the clamped boundary conditions, the back part of the battery and a small part of the main body entered the cockpit. For the thinner windshield with the alternative boundary conditions, only the front part of the main body and of the battery did not penetrate the windshield. In case the alternative boundary conditions would be an appropriate representation of the surrounding structure of the windshield, the cockpit crew would be exposed to a significantly higher risk of sustaining injuries due to parts of the UAS striking the body. This would compromise the level of safety for the crew and passengers even further.

3. Bird strike comparison

As mentioned above, the windshields of a Part 29 rotorcraft are designed to comply with a bird strike requirement. The results of the UAS impact simulations showed that this compliant windshield would sustain severe damage after an impact with a DJI Phantom III. When comparing the results of the simulations, it becomes apparent that the damage mechanism differs between a bird strike and UAS impact. To emphasize this difference, the damage initiation and final damage of a windshield impacted by the bird and by the UAS are shown in Figure 10. The thicknesses of the windshields was selected such that the resulting final damage caused by these impacts was of a comparable size.

After the UAS battery and camera made contact with the windshield, the damage instantly initiated at the impact location. The components of the UAS partly bounced off and partly penetrated the windshield, thereby concentrating the load at the impact location. Thereafter, the damage propagated and created a distinct hole in the middle of the windshield whilst the edges of the windshield remained intact. The bird initially contacted the windshield at the same location as the battery of the UAS. However, the bird did not bounce off the windshield, but deformed and flowed along the inclination of the target. This resulted in the load extending over a larger area. The damage was subsequently initiated at the top of the windshield and thereafter propagated further downwards over the windshield. At the end of the simulation, the left hand side and bottom edge of the windshield remained intact. In this simulation, the bird partly penetrated the cockpit through the opening that was created at the top edge of the windshield after the damage initiation.

The comparison of the impact events showed that the design of the windshield takes into account a soft body damage propagation mechanism whilst the UAS impact can be considered a hard body impact. To guarantee crew and passengers safety after an impact by a UAS, the certification requirements of the windshield should be amended to incorporate an appropriate hard body impact criteria. To comply with such a requirement, a different philosophy should be adopted during the design phase of the windshield. Suggestions for this purpose would be to replace the standard acrylic windshield by tougher materials such as high quality polycarbonate or incorporate a laminated glass lay-up.

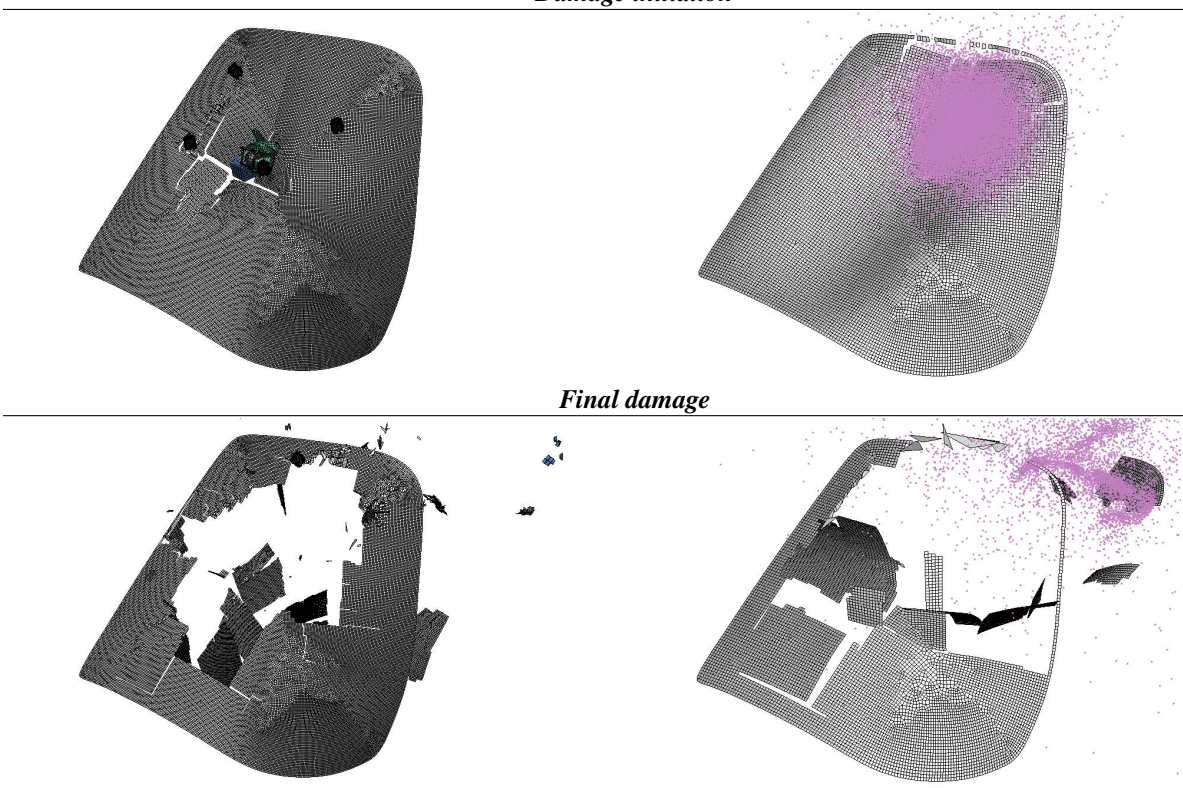

(a) UAS impact on a 9.3 mm thick windshield. UAS main body is not shown.

(b) Bird strike on a 7.0 mm thick windshield.

Fig. 10 Comparison of the damage propagation mechanism of a windshield UAS impact and bird strike.

V. Conclusion

The current state of art focused on assessing the damage that a fixed wing aircraft would sustain after colliding with a UAS. However since helicopters regularly fly within the airspace where UAS operators are permitted to fly their device without approval of the operation, the manned helicopter operator is certainly not retained from the risk of colliding with a UAS. Due to the fact that the certification requirements, operating conditions, and design philosophy of a helicopter differ from fixed wing aircraft, the risk a helicopter operator faces regarding the UAS collision remained unknown. The outcome of this paper predicts the damage that a helicopter would sustain following an encounter with a UAS and provides additional insight in the risk helicopter occupants face at this moment.

The results of the various simulations in this paper show that a Part 29 compliant windshield would sustain severe damage after a collision with the DJI Phantom III. The safety of the passengers and crew could not be guaranteed following the impact due to fragments of the windshield as well as parts of the UAS entering the cockpit and potentially severely injuring the crew. It is worth emphasizing that no impact related certification requirement is imposed on the smaller Part 27 rotorcraft. Therefore, a thinner windshield would suffice to pass certification of these aircraft resulting in even more severe damage and more parts of the UAS penetrating the cockpit after the collision.

Based on the simulations, the risk that the passengers and crew of the rotorcraft face whilst sharing airspace with UAS operators becomes apparent. Following this conclusion, the question arises as to how this risk can be reduced and the answer to this question is twofold. On one hand, the chance of the collision can potentially be eliminated by imposing and subsequently enforcing stricter regulations on UAS operations or adopting a solid collision avoidance system. On the other hand if the chance of a collision remains present, the design of the rotorcraft should be changed such that safety of the rotorcraft occupants is guaranteed after the collision. For this purpose, the certification requirements should be amended to incorporate a hard body impact criteria for both the Part 27 and Part 29 compliant helicopters.

An opportunity for further work is to incorporate an accurate representation of the surrounding structure of the

windshield in the simulations, since the comparison of the two sets of boundary conditions showed that the damage is sensitive to the imposed boundary conditions. The research can also be further elaborated on by simulating the sustained damage of an impact onto other helicopter components such as the flight critical main rotor blades or to simulate collisions with other types of UAS compared to the quadcopter DJI Phantom III. For example fixed wing UAS have a different design and generally fly at higher velocities, which potentially could cause more sustained damage to the rotorcraft.

References

[1] Meola A, "Drone market shows positive outlook with strong industry growth and trends", *Business Insider of July 13*, 2017, http://www.businessinsider.com/drone-industry-analysis-market-trends-growth-forecasts-2017-7 [Accessed March 2019].

[2] Federal Aviation Administration, "Small unmanned aircraft systems", 14 CFR §107, 2019, https://www.ecfr.gov [Accessed May 2019].

[3] Gilbert G, "UK Report: Drone proximity incidents double", *Aviation International News of November 30*, 2017, https://www.ainonline.com/aviation-news/business-aviation/2017-11-30/uk-report-drone-proximity-incidents-double [Accessed May 2019].

[4] Federal Aviation Administration, (2019b), "Airworthiness Standards: Transport Category Aircraft", 14 CFR §29, 2019, https://www.ecfr.gov [Accessed May 2019].

[5] European Aviation Safety Agency, "Certification Specifications and Acceptable Means of Compliance for Large Rotorcraft", CS-29 Amendment 6, 2018, https://www.easa.europa.eu/regulations#regulations-initial-airworthiness [Accessed May 2019].

[6] Livermore Software Technology Corporation, "LS-Dyna keyword user's manual", Revision 11, 2018.

[7] GrabCAD, "DJI Phantom III CAD Model", 2015, https://grabcad.com/library/dji-phantom3-1 [Accessed November 2019].

[8] Metallic Material Properties Development Standardization, "MMPDS Chapter 9", Ed. 7, Battelle Memorial Institute, Washington D.C., 2014.

[9] Sahraei A, Meier J, Wierzbicki T, "Characterizing and modeling mechanical properties and on- set of short circuit for three types of lithium-ion pouch cells", *Elsevier Journal of Power Sources*, Vol. 247, 2014, pp.503-516.

[10] Meng X, Sun Y, Yu J, Tang Z, Liu J, Suo T, Li Y, "Dynamic response of the horizontal stabilizer during UAS airborne collision", *Elsevier International Journal of Impact Engineering*, Vol. 126, 2018, pp.50-61.

[11] Olivares G, Gomez L, Espinosa de los Monteros J, Baldridge RJ, Zinzuwadia C, Aldag T, "UAS Airborne collision severity evaluation - Volume II - Quadcopter", Report DOT/FAA/AR-xx/xx, Federal Aviation Administration, Washington D.C., 2017.

[12] Kay G, "Failure modeling of titanium 6AI-4V and aluminium 2024-T3 with the Johnson-Cook material model", Report DOT/FAA/AR-03/57, Federal Aviation Administration, Washington D.C., 2003.

[13] GrabCAD, "Augusta A-109 CAD Model", 2014, https://grabcad.com/library/augusta-a-109-1 [Accessed October 2019].

[14] Hedayati R, Ziaei-Rad S, Eyvazian A, Hamouda AM, "Bird strike analysis on a typical helicopter windshield with different lay-ups", *Springer Journal of Mechanical Science and Technology*, Vol. 28 (4), 2014, pp.1382-1392.

[15] Grimaldi A, "SPH high velocity impact analysis: A birdstrike windshield application", PhD dissertation University of Naples Federico II, 2011, http://dx.doi.org/10.6092/UNINA/FEDOA/8221.